

Article

Low-Temperature-Tolerant Aqueous Proton Battery with Porous $\text{Ti}_3\text{C}_2\text{T}_x$ MXene Electrode and Phosphoric Acid Electrolyte

Jun Zhu ¹, Xude Li ¹, Bingqing Hu ¹ , Shanghai Ge ^{2,*} and Jiang Xu ^{1,*}¹ School of Mechanical Engineering, Jiangsu University, Zhenjiang 212013, China; zhujzzy@ujs.edu.cn (J.Z.); 2222103175@stmail.ujs.edu.cn (X.L.); 2112003005@stmail.ujs.edu.cn (B.H.)² Department of Mechanical Engineering, The Pennsylvania State University, University Park, PA 16802, USA

* Correspondence: sug13@psu.edu (S.G.); xuj@yzu.edu.cn (J.X.)

Abstract: Supercapacitors have long suffered from low energy density. Here, we present a high-energy, high-safety, and temperature-adaptable aqueous proton battery utilizing two-dimensional $\text{Ti}_3\text{C}_2\text{T}_x$ MXenes as anode materials. Additionally, our work aims to provide further insights into the energy storage mechanism of $\text{Ti}_3\text{C}_2\text{T}_x$ in acid electrolytes. Our findings reveal that the ion transport mechanism of $\text{Ti}_3\text{C}_2\text{T}_x$ remains consistent in both H_2SO_4 and H_3PO_4 electrolytes. The mode of charge transfer depends on its terminal groups. Specifically, the hydrogen bonding network formed by water molecules adsorbed by hydroxyl functional groups under van der Waals forces enables charge transfer in the form of naked H^+ through the Grotthuss mechanism. In contrast, the hydrophobic channel formed by oxygen and halogen terminal groups facilitates rapid charge transfers in the form of hydronium ion via the vehicle mechanism, owing to negligible interfacial effect. Herein, we propose an aqueous proton battery based on porous hydroxy-poor $\text{Ti}_3\text{C}_2\text{T}_x$ MXene anode and pre-protonated $\text{Cu}^{II}[\text{Fe}^{III}(\text{CN})_6]_{2/3}\cdot 4\text{H}_2\text{O}$ (H-TBA) cathode in a 9.5 M H_3PO_4 solution. This proton battery operates through hydrated H^+/H^+ transfer, leading to good electrochemical performance, as evidenced by 26 Wh kg⁻¹ energy density and 162 kW kg⁻¹ power density at room temperature and an energy density of 17 Wh kg⁻¹ and a power density of 7.4 kW kg⁻¹ even at -60 °C.

Keywords: proton battery; MXene; low-temperature tolerant; grotthuss mechanism

Citation: Zhu, J.; Li, X.; Hu, B.; Ge, S.; Xu, J. Low-Temperature-Tolerant Aqueous Proton Battery with Porous $\text{Ti}_3\text{C}_2\text{T}_x$ MXene Electrode and Phosphoric Acid Electrolyte. *Batteries* **2024**, *10*, 207. <https://doi.org/10.3390/batteries10060207>

Academic Editor: Xianyong Wu

Received: 14 May 2024

Revised: 7 June 2024

Accepted: 9 June 2024

Published: 14 June 2024



Copyright: © 2024 by the authors. Licensee MDPI, Basel, Switzerland. This article is an open access article distributed under the terms and conditions of the Creative Commons Attribution (CC BY) license (<https://creativecommons.org/licenses/by/4.0/>).

1. Introduction

Electrochemical capacitors, also called supercapacitors, are energy storage devices that are capable of both delivering high power and sustaining long-term service compared to Li^+ batteries [1,2]. Currently, electric double-layer capacitors (EDLCs) using activated carbon as the electrode material dominate the supercapacitor market. Despite offering high-power density, EDLCs suffer from limited energy density, typically below 10 Wh kg⁻¹, even when employing organic electrolytes [3]. This limitation arises because the capacitance of EDLCs primarily originates from the electron-sorption of ions at the electrode/electrolyte interface [3,4]. In contrast, an alternative subclass of supercapacitor, pseudo-capacitor, offers a route to store more charges than porous carbon through Faradaic reactions [4,5]. For example, common transition metal oxides [6–8] and conductive polymers [9,10] could theoretically provide specific capacity ranging from hundreds to over one thousand C g⁻¹ via reversible surface redox reactions. However, low electrical conductivity and sluggish ion diffusion in the bulk active material have stifled power performance and limited the utilization of their theoretical storage capacity thus far [7,9]. Although various approaches such as the addition of conductive agents (e.g., carbon nanomaterials [11] and nanoporous metal [12]), the reduction in particle size [13], and the fabrication of metal-organic frameworks [14] have been adopted to alleviate the aforementioned issues, they may inadvertently introduce new issues, such as an increase in the mass of non-active material and a decrease in electrode density. Consequently, these strategies often yield only moderate improvements.

In recent years, a family of two-dimensional (2D) transition metal carbides/nitrides (MXene) has been identified as materials for pseudo-capacitive capacitors due to their unique characteristics. These include high electronic conductivity, high surface area, and abundant active sites [15]. Up to now, researchers have synthesized more than 30 different MXenes [16]. Among these, $\text{Ti}_3\text{C}_2\text{T}_x$ stands out as the most extensively studied MXene. It has been proven to be a suitable material for cation intercalation [17,18]. In particular, $\text{Ti}_3\text{C}_2\text{T}_x$ hydrogel film, when used as an electrode in H_2SO_4 solution, has achieved a volumetric capacitance of 1500 F cm^{-3} [19].

It is widely acknowledged that $\text{Ti}_3\text{C}_2\text{T}_x$ MXenes are primarily used as anodes in supercapacitors and batteries [10,20]. To maintain the high volumetric capacitance of the MXene anode, a cathode with equally high volumetric capacitance is essential. It will raise new challenges. First, it is difficult for large-sized anions to transport in dense pseudo-capacitive materials [13]. Second, the amount of electrolyte is limited. Once a large number of ions are adsorbed, their concentration will sharply decrease, severely limiting device applications at low temperatures. Therefore, maximizing the performance of MXenes requires additional considerations such as ionic resource, conductivity, and diffusion for designing practical devices beyond supercapacitors.

Aqueous proton batteries offer a potential solution because the proton (H^+) has the smallest size and the lightest weight among all cation ions [21,22]. However, the naked H^+ can rarely be used as a charge carrier because of the formation of H_3O^+ , which has high dehydration energy (11.66 eV, $\text{H}_3\text{O}^+ \rightarrow \text{H}^+ + \text{H}_2\text{O}$) [23]. Namely, H_3O^+ can generally be used as a charge carrier rather than the naked H^+ unless there is a continuous hydrogen bonding network in the active electrode [24,25]. Compared to lithium-ion batteries, supercapacitors exhibit excellent rate performance, making it possible for them to work well at low temperatures. However, the decrease in temperature significantly reduces ion transport in the supercapacitor and desolvation at the solid/liquid interface [26,27]. Notably, the highest capacitance of MXenes is obtained in H_2SO_4 electrolyte, ensuring ion transport even at low temperatures [15]. Nevertheless, the use of highly concentrated H_2SO_4 increases security concerns for the device.

Recently, Jiang et al. demonstrated that highly concentrated H_3PO_4 could serve as the electrolyte for proton batteries (Table S1). The high compatibility between H_3PO_4 and MoO_3 anode ensures appreciable power performance at and below -78°C [28]. However, the compatibility between H_3PO_4 and MXene anode, especially at extremely low temperatures, and the impact of anions on proton diffusion are still unclear.

Previous studies have utilized several in situ techniques to investigate the charge storage mechanism of $\text{Ti}_3\text{C}_2\text{T}_x$. In situ X-ray absorption spectroscopy measurements have shown a change in the oxidation state of Ti during electrochemical polarization in H_2SO_4 electrolyte [29]. In situ XRD measurements have confirmed that the charge storage mechanism involves intercalation pseudo-capacitance [30]. In addition, density functional theory (DFT) calculations have been used to describe the pseudo-capacitive behavior of $\text{Ti}_3\text{C}_2\text{T}_x$ in acid electrolyte [31].

Although considerable efforts have been made to understand the charge storage mechanisms of MXenes, several questions still need to be addressed, especially regarding how hydrogen ions transport in two-dimensional MXenes, which will affect the modification of electrode material and the design of energy storage devices. In this work, we have first combined electrochemical quartz crystal microbalance tests in acid electrolytes for a wide potential window and molecular dynamics (MD) simulations to further investigate the charge transfer mechanism of the $\text{Ti}_3\text{C}_2\text{T}_x$ in acid electrolytes. Our findings confirm that the ion transport mechanisms in $\text{Ti}_3\text{C}_2\text{T}_x$ are the same in H_2SO_4 and H_3PO_4 electrolytes; both proton (Grutthuss mechanism) and hydronium ion (Vehicle mechanism) transfer exist during charge and discharge due to differences in terminal groups. This consistent energy storage mechanism enables porous hydroxy-poor $\text{Ti}_3\text{C}_2\text{T}_x$ MXene || pre-protonated $\text{Cu}^{II}[\text{Fe}^{III}(\text{CN})_6]_{2/3} \cdot 4\text{H}_2\text{O}$ (H-TBA) proton battery to exhibit excellent rate and low-temperature performance.

2. Materials and Methods

Preparation of few-layer $Ti_3C_2T_x$ colloidal solution: The synthesis of multilayered $Ti_3C_2T_x$ involved etching Ti_3AlC_2 powders (400 mesh, 11 Technology Co., Ltd., Jilin, China), following a method similar to that reported in our previous study [15]. The remaining sediment (multilayer $Ti_3C_2T_x$) was dispersed in 100 mL of deionized water and subjected to probe sonication (power: 400 W) for 60 min under Ar flow and an ice bath. After centrifugation at 3500 rpm for 60 min, the resulting supernatant was collected to obtain the few-layer $Ti_3C_2T_x$ colloidal solution. The concentration of the colloidal solution was determined by filtering a known volume and measuring the weight of the dried film after vacuum drying [19].

Fabrication of vacuum-filtered $Ti_3C_2T_x$ MXene film: The $Ti_3C_2T_x$ colloidal solution was vacuum filtered through a Celgard 3501 polypropylene membrane. The resulting film on the polypropylene membrane was collected and dried overnight in a vacuum oven at 80 °C. Afterward, a flexible, free-standing $Ti_3C_2T_x$ thin film was obtained by peeling the thin film off the polypropylene membrane. Finally, the film was pressed on a smooth Cu foil under a pressure of 2 MPa.

Fabrication of porous $Ti_3C_2T_x$ MXene (PS-MXene) film: The polystyrene spheres (PS) were polymerized from styrene, as reported by Park et al. [32]. Then, the delaminated $Ti_3C_2T_x$ MXene colloidal solution was sonicated with PS spheres (the mass ratio of PS to MXene was 3:1) for 10 min to form a uniform dispersion. The colloidal mixture solution was vacuum filtered onto the polypropylene membrane and then vacuum-dried overnight at 80 °C. A free-standing PS-MXene film was peeled off from the polypropylene membrane and annealed at 400 °C under Ar flow for 1 h. After annealing, a free-standing templated porous $Ti_3C_2T_x$ MXene film was prepared. Finally, the film was pressed on a smooth Cu foil under a pressure of 2 MPa.

Preparation of chemically pre-protonated Turnbull's blue analogue (H-TBA): H-TBA was synthesized by the chemical reduction of $Cu^{II}[Fe^{III}(CN)_6]_{2/3} \cdot 4H_2O$ (denoted as CuFe-TBA) [28].

Materials characterization: X-ray diffraction (XRD) patterns were collected on an advanced powder X-ray diffractometer (Bruker D8) equipped with copper K α radiation ($\lambda = 1.54 \text{ \AA}$). The cross-sections and elementary compositions of the MXene films were characterized by a JSM-IT800 field emission scanning electron microscope (FE-SEM, JOEL) equipped with an energy-dispersive X-ray spectroscope (EDS, Oxford). The atomic-resolution characterization of the $Ti_3C_2T_x$ MXene was conducted on a scanning transmission electron microscope (STEM, Thermo Fisher Titan Themis G2 60-300) operated at 300 kV. Single-layer $Ti_3C_2T_x$ for high-angle annular dark-field (HAADF) STEM observation was prepared by dropping two drops of the diluted $Ti_3C_2T_x$ colloidal solution onto a lacey carbon-coated copper grid (Beijing XXBR Technology Co., Ltd., China) and drying with Ar flow. Foil samples of the vacuum-filtered $Ti_3C_2T_x$ MXene film for cross-section STEM observation were prepared using a Zeiss Crossbeam 540 focused ion beam. Chemical compositions of $Ti_3C_2T_x$ MXene were further analyzed by ESCALAB 250Xi X-ray photoelectron spectroscopy (XPS, Thermo Fisher Scientific, Waltham, MA, USA). Peak fitting was carried out using Thermo Avantage software (v5.9921).

Electrochemical quartz crystal microbalance (EQCM) tests. For the sample preparation of EQCM, the diluted $Ti_3C_2T_x$ colloidal solution was drop-coated on the surface of Au-coated quartz crystals with an oscillating frequency of 5 MHz (Shenzhen RenLux Crystal Co., Ltd, Shenzhen, China.). After drying at room temperature overnight with N₂ flow, the resulting ultrathin binder-free $Ti_3C_2T_x$ film had solid adhesion to the Au-coated quartz crystals and was used as the working electrode. The measurements were performed in a three-electrode system, where Ag/AgCl in saturated KCl and activated carbon were used as reference and counter electrodes, respectively. The electrolytes were 5 M H₂SO₄ and 9.5 M H₃PO₄, respectively. All EQCM electrochemical measurements were performed using an electrochemical quartz crystal microbalance (eQCM 10M, Gamry, Philadelphia, PA, USA) and an electrochemical workstation (Reference 3000, Gamry).

Electrode preparation: In three-electrode tests, the activated carbon (AC) electrode was used as a counter electrode and prepared by the mechanical processing of a pre-mixed slurry containing 90 wt.% YP-50 AC (Kuraray, Japan), 5 wt.% Ketjen black (ECP600JD, Lion Specialty Chemicals Co., Ltd.), and 5 wt.% polytetrafluoroethylene (DAIKIN, Japan) binder in ethanol. The mass loading of the obtained electrode was $\sim 15 \text{ mg cm}^{-2}$. To avoid the failure of the Ag/AgCl electrode during low-temperature tests, the AC electrode was pressed on platinum mesh and served as the reference electrode [15]. In two-electrode tests, a mixture slurry containing 70 wt.% H-TBA powder, 20 wt.% Ketjen carbon, and 10 wt.% polyvinylidene fluoride binder (PVDF, Solvay (Shanghai) Co., Ltd., Shanghai, China) was coated on carbon fiber paper current collector to serve as a cathode.

Electrochemical tests: All electrochemical tests were performed in three-electrode Swagelok cells using glass carbon as a current collector. For three-electrode tests at room temperature, Ag/AgCl in saturated KCl and Celgard 3501 membrane were used as the reference electrode and separator, respectively. In low-temperature tests, the reference electrode was replaced by an AC electrode. The electrolytes used were 5 M H_2SO_4 and 9.5 M H_3PO_4 , respectively. For full cell tests, the masses of the active materials in PS-MXene and H-TBA were set at 0.7 and 0.75 mg cm^{-2} , respectively. Cyclic voltammetry (CV), electrochemical impedance spectroscopy (EIS), and galvanostatic charge/discharge (GCD) were performed on CHI660E electrochemical workstation. The electrode underwent an initial pre-cycling process consisting of 10 cycles at 2 mV s^{-1} . Following this, CV was performed with scan rates ranging from 2 to 100 mV s^{-1} . GCD was performed at current densities from 1 to 200 A g^{-1} . EIS was performed in a frequency range from 10^{-2} to 10^5 Hz with an amplitude of 5 mV. The electrochemical tests at different temperatures were performed in a high-/low-temperature test chamber (GP/T-150, Guangpin Test Equipment Manufacturing Co. Ltd., Shanghai, China).

Calculations: All the calculations based on DFT are performed by Vienna Ab initio Simulation Package (VASP). The projector augmented wave (PAW) pseudo-potentials with the Perdew–Burke–Enrnerhof (PBE) functional were used. The cutoff of kinetic energy was set as 500 eV, and to eliminate the physical interactions caused by periodic boundary conditions, the vacuum spaces were larger than 20 \AA . In total, we used 3×3 supercells to simulate the adsorptions of water molecule on the $\text{Ti}_3\text{C}_2\text{X}_2$ ($\text{X}=\text{O}, \text{F}, \text{Cl}, \text{OH}$) surface. The force and energy convergence criteria were set to $0.001 \text{ eV \AA}^{-1}$ and 10^{-5} e \AA , respectively. The adsorption energy of molecules on the surface was defined as follows:

$$E_{\text{ads}} = E_{\text{total}} - E_{\text{Ti}_3\text{C}_2\text{X}_2} - E_{\text{molecule}} \quad (1)$$

where E_{ads} denotes the adsorption energy, E_{total} is the total energy of water molecule adsorbed on $\text{Ti}_3\text{C}_2\text{X}_2$, and $E_{\text{Ti}_3\text{C}_2\text{X}_2}$ and E_{molecule} represent the energy of pure $\text{Ti}_3\text{C}_2\text{X}_2$ and water molecule, respectively.

3. Results and Discussion

3.1. Characterization of $\text{Ti}_3\text{C}_2\text{T}_x$ MXene

Previous studies have highlighted the importance of the structure, particularly the surface state, in determining the energy storage capabilities of MXene [16,33,34]. In this work, several key characterizations of $\text{Ti}_3\text{C}_2\text{T}_x$ MXene were conducted. To produce the few-layer $\text{Ti}_3\text{C}_2\text{T}_x$ colloidal solution, we used a relatively low-toxicity HCl+LiF solution to etch Ti_3AlC_2 , followed by an ultrasonic-assisted exfoliation method (Scheme S1). The resulting diluted few-layer $\text{Ti}_3\text{C}_2\text{T}_x$ colloidal solution appears dark green and displays the ‘Tyndall’ effect (Figure S1a). In addition, a freestanding film electrode was fabricated through vacuum filtration, exhibiting excellent flexibility (Figure S1b).

The XRD pattern of the $\text{Ti}_3\text{C}_2\text{T}_x$ film does not show peaks corresponding to Ti_3AlC_2 , indicating the successful synthesis of pure $\text{Ti}_3\text{C}_2\text{T}_x$ MXene film (Figure 1a). This is further validated by HAADF STEM images of the monolayer and cross-section $\text{Ti}_3\text{C}_2\text{T}_x$ MXene at atomic level resolution (Figure 1b,c). EDS reveals a uniform distribution of various elements, with the atomic ratio of oxygen being higher than that of halogens (F and Cl,

Figure 1e). Furthermore, the high-resolution XPS spectra of O 1s and Ti 2p further indicate that the oxygen element is mainly contributed by hydroxyl groups (Figure 1f,g). Thus, the presence of abundant hydroxyl terminal groups would enable the adsorption of a large number of water molecules into the interlayer of MXene, causing an increase in interlayer spacing [35]. Compared with pure water, the interlayer spacing of the $\text{Ti}_3\text{C}_2\text{T}_x$ film in acid electrolyte is reduced (Figure 1d). This could be attributed to the positively charged H^+ ions intercalated between negatively charged $\text{Ti}_3\text{C}_2\text{T}_x$ layers, increasing the electrostatic attraction between the layers [30]. Therefore, compared to the previous report of cation intercalation into $\text{Ti}_3\text{C}_2\text{T}_x$, which showed reversible and continuous shifts, [17] the mechanism of H^+ intercalation appears to be more complex.

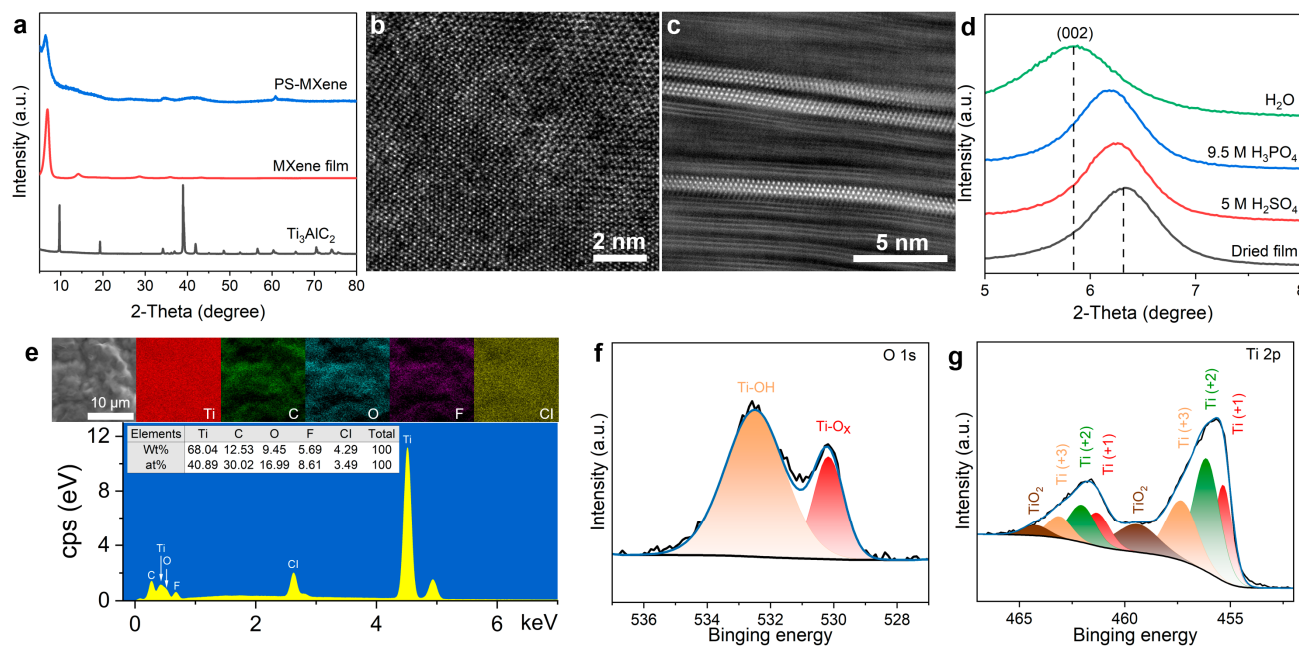


Figure 1. Characterization of $\text{Ti}_3\text{C}_2\text{T}_x$ MXene. (a) XRD patterns of Ti_3AlC_2 powder, vacuum-filtered MXene film, and porous $\text{Ti}_3\text{C}_2\text{T}_x$ MXene film (PS-MXene). (b) HAADF STEM image of the monolayer $\text{Ti}_3\text{C}_2\text{T}_x$ viewed along the $[0001]$ direction. (c) Cross-section HAADF STEM image of the $\text{Ti}_3\text{C}_2\text{T}_x$ film. (d) XRD patterns of the dried $\text{Ti}_3\text{C}_2\text{T}_x$ film and the corresponding films immersed in H_2O , 9.5 M H_3PO_4 , and 5 M H_2SO_4 , respectively. (e) EDS elemental mappings and analysis of $\text{Ti}_3\text{C}_2\text{T}_x$ MXene film. High-resolution XPS spectra of (f) O 1s and (g) Ti 2p of the $\text{Ti}_3\text{C}_2\text{T}_x$ film.

3.2. Hydrogen Ion Transport Mechanism in $\text{Ti}_3\text{C}_2\text{T}_x$ MXene

To elucidate the charge storage and transport mechanism, we conducted EQCM studies using a $\text{Ti}_3\text{C}_2\text{T}_x$ MXene-coated gold quartz crystal in acid electrolytes. This EQCM technique enables the *operando* gravimetric tracking of change in the working electrode, offering valuable insight into ion fluxes during electrochemical polarization [36]. We selected a suitable potential window (-0.25 to 0.25 V vs. Ag/AgCl) to encompass the pseudo-capacitive reaction part while simultaneously avoiding H_2 evolution during the experiment. The CV profile and mass response of $\text{Ti}_3\text{C}_2\text{T}_x$ at 10 mV s^{-1} shows an overlap of the start and end points of the mass scan loop, indicating steady and reversible charge-transfer within this voltage range regardless of whether the MXene is in 5 M H_2SO_4 or 9.5 M H_3PO_4 electrolyte (Figure 2a,b). This indicates its potential for various electrochemical energy storage applications. Additionally, the observed weak hysteresis between positive and negative scans is likely attributed to kinetic limitations.

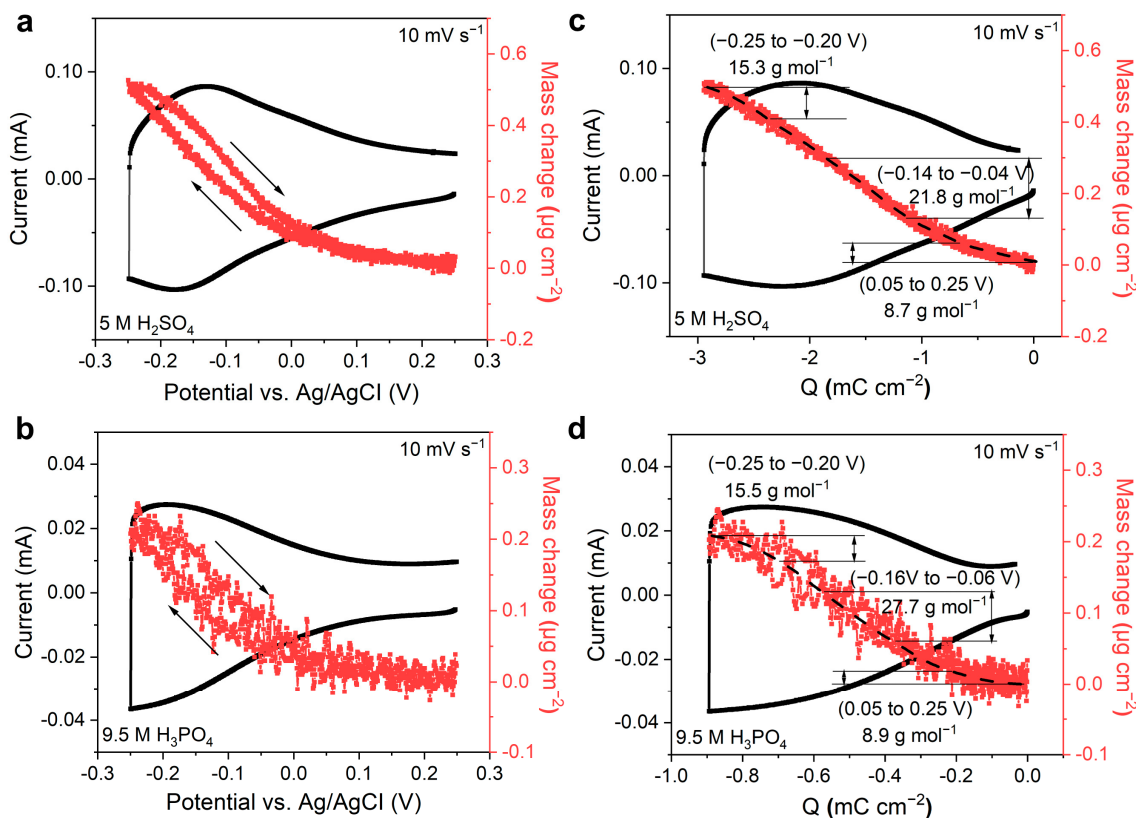


Figure 2. EQCM test of $\text{Ti}_3\text{C}_2\text{T}_x$ MXene in acid electrolytes. CV profile and electrode mass response for $\text{Ti}_3\text{C}_2\text{T}_x$ MXene in (a) 5 M H_2SO_4 and (b) 9.5 M H_3PO_4 . Electrode mass change versus charge for $\text{Ti}_3\text{C}_2\text{T}_x$ MXene in (c) 5 M H_2SO_4 and (d) 9.5 M H_3PO_4 . The $\text{Ti}_3\text{C}_2\text{T}_x$ MXene is coated on an Au-coated quartz crystals substrate. Scan rate is set at 10 mV s^{-1} and potential range is set as -0.25 to 0.25 V .

It is noted that the mass change versus accumulated charge exhibits similar behavior in both 5 M H_2SO_4 and 9.5 M H_3PO_4 electrolytes (Figure 2c,d). This suggests that the charge storage and transport mechanism are consistent in these two electrolytes. Within the working voltage for the electric double layer, spanning from 0.05 to 0.25 V (vs. Ag/AgCl), a nearly linear increase in mass versus accumulated charge is observed (Figure S2). By applying Faraday's law, the average molecular weight per charge is 9 g mol^{-1} , approximately half of H_3O^+ (19 g mol^{-1}), indicating the transport of both naked H^+ and hydronium ions during charging/discharging. During redox reactions, the ratio of mass to accumulated charge gradually increases, reaching approximately 21.8 and 27.7 g mol^{-1} within the potential range of -0.14 to -0.04 V (vs. Ag/AgCl) in 5 M H_2SO_4 and 9.5 M H_3PO_4 electrolytes, respectively. This suggests the presence of hydronium ions with a higher number of water molecules (e.g., H_5O_2^+ or H_7O_3^+). Further decreasing the potential window to the range of -0.25 to -0.20 V (vs. Ag/AgCl) leads to a decrease in the ratio of mass to accumulated charge to about 15.5 g mol^{-1} in both electrolytes. These findings indicate that the ratio of mass to accumulated charge does not increase gradually with an increase in pseudo-capacitance ratio.

DFT and MD calculations were employed to explore the charge storage and transport mechanism of $\text{Ti}_3\text{C}_2\text{T}_x$ in acid electrolytes. It was observed that the hydroxyl terminal group demonstrates greater hydrophilicity compared to the oxygen and halogen terminal groups (Figure S3). A large number of water molecules tend to be adsorbed by hydroxyl terminal groups with the layers (Figure 3a). Under the action of van der Waals forces, these adsorbed water molecules become confined and form a continuous hydrogen bonding network. Thus, the naked H^+ could transfer in the layer through the Grotthuss mechanism, as shown in Figure 3b. Meanwhile, for hydrophobic channels formed by oxygen and halogen

terminal groups (Figure 3c), the hydronium ions can transfer in the layer directly through the Vehicle mechanism (Figure 3d). Therefore, in the initial electric double-layer region, the predominance of naked H^+ compared to hydronium ions leads to the lowest molecular weight per charge. However, as the redox reaction initiates, this ratio diminishes rapidly, causing a subsequent rise in the molecular weight per charge. As the reaction progresses, a large number of hydronium ions become confined within the layer, thereby facilitating an enhancement of the hydrogen bonding network where these ions are chemically adsorbed onto the reduced Ti-O active sites [15,19]. Consequently, this phenomenon leads to a decrease in the molecular weight per charge. Based on the above analysis, it can be deduced that the ion transport and storage mechanisms of $Ti_3C_2T_x$ in H_2SO_4 and H_3PO_4 electrolytes are similar.

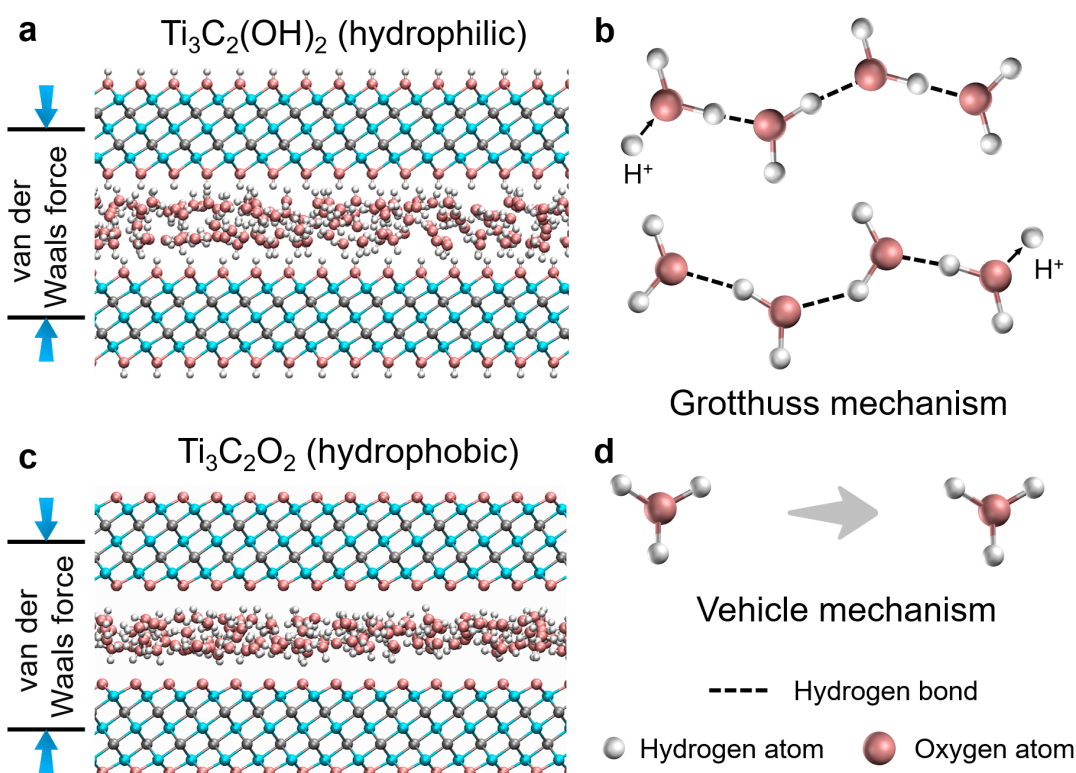


Figure 3. Hydrogen ion transport in $Ti_3C_2T_x$ MXene. (a) Simulation of the H_2O molecules confined in the hydrophilic channel of $Ti_3C_2(OH)_2$. (b) Schematic of the Grotthuss mechanism, depicting proton conduction through the rearrangement of bonds along a water chain in the channel of $Ti_3C_2(OH)_2$. (c) Simulation of the H_2O molecules confined in the hydrophobic channel of $Ti_3C_2O_2$. (d) Schematic depiction of the Vehicle mechanism, showing the migration of the hydrated hydrogen ion as a whole along the channel of $Ti_3C_2O_2$.

3.3. Proton Battery Based on Porous $Ti_3C_2T_x$ MXene in H_3PO_4 Electrolyte

To verify the feasibility of $Ti_3C_2T_x$ in H_3PO_4 electrolyte, CV tests were conducted, and electrochemical performances were compared in both H_2SO_4 and H_3PO_4 electrolytes (Figure 4a). The results show that $Ti_3C_2T_x$ performs well in 9.5 M H_3PO_4 electrolytes, exhibiting a specific capacitance comparable to that measured in 5 M H_2SO_4 . Furthermore, it exhibits good rate performance in 9.5 M H_3PO_4 (Figure 4b and Figure S4). Although the specific capacitance in 9.5 M H_3PO_4 is a little lower than that in 5 M H_2SO_4 at high scan rates ($>10\text{ mV s}^{-1}$), it maintains more than 60% capacitance at 100 mV s^{-1} (Figure 4c). The reduction in rate performance might be attributed to the high viscosity and poor wettability, leading to increased diffusion resistance (Figure 4d) [37]. Moreover, with decreasing temperature, resistance increases significantly (Figures 4e and S5), resulting in

decreased specific capacity from 72 mAh g^{-1} at 20°C to 17 mAh g^{-1} at -60°C even at 1 A g^{-1} (Figures 4f and S6).

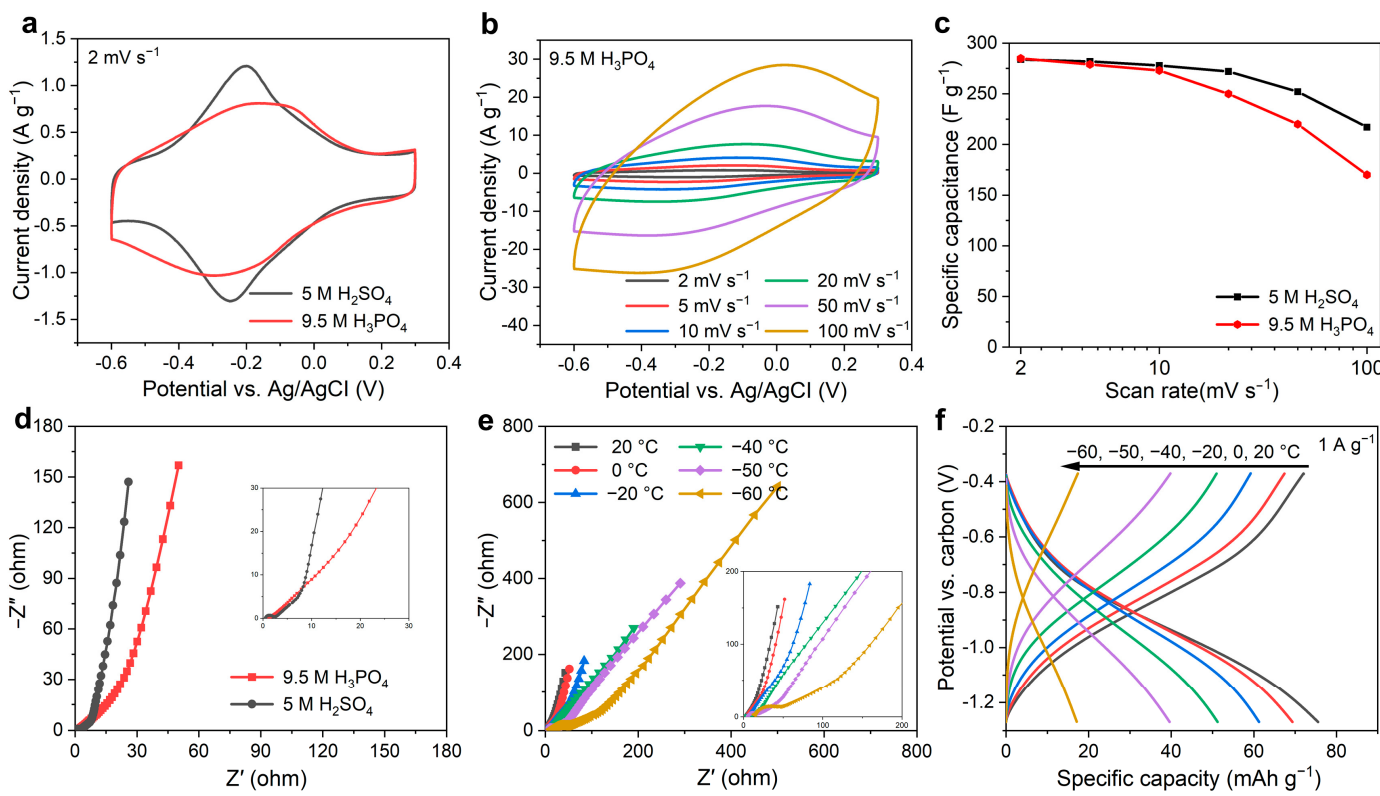


Figure 4. Electrochemical characterization of the $\text{Ti}_3\text{C}_2\text{T}_x$ film electrode in acid electrolyte. CV plots of the $\text{Ti}_3\text{C}_2\text{T}_x$ film measured (a) at 2 mV s^{-1} in both $5 \text{ M H}_2\text{SO}_4$ and $9.5 \text{ M H}_3\text{PO}_4$, and (b) at different scan rates in $9.5 \text{ M H}_3\text{PO}_4$ electrolyte. (c) Gravimetric rate performance of the $\text{Ti}_3\text{C}_2\text{T}_x$ film electrode calculated from CV at different scan rates in both $5 \text{ M H}_2\text{SO}_4$ and $9.5 \text{ M H}_3\text{PO}_4$. (d) EIS data of the $\text{Ti}_3\text{C}_2\text{T}_x$ film collected at 0.2 V vs. Ag/AgCl in both $5 \text{ M H}_2\text{SO}_4$ and $9.5 \text{ M H}_3\text{PO}_4$ electrolyte. (e) EIS data of the $\text{Ti}_3\text{C}_2\text{T}_x$ film electrode collected at -0.45 V vs. carbon for different temperatures in $9.5 \text{ M H}_3\text{PO}_4$. (f) Galvanostatic cycling profiles of the $\text{Ti}_3\text{C}_2\text{T}_x$ film at different temperatures with 1 A g^{-1} in $9.5 \text{ M H}_3\text{PO}_4$ electrolyte. The insets of (d,e) show the high-frequency range.

To relieve the issue of poor wettability and sluggish ion transfer in vacuum-filtered film characterized by a brick-wall structure, a porous $\text{Ti}_3\text{C}_2\text{T}_x$ MXene film was developed using polystyrene (PS) spheres as a templet, followed by annealing and pressing steps. Initially, $\text{Ti}_3\text{C}_2\text{T}_x$ MXene was evenly distributed on the surface of PS spheres (Figure 5a). After annealing, the PS spheres were removed, leaving a well-defined porous structure (Figure 5b). These pores collapsed and formed numerous channels after pressing, which could improve wettability and shorten the ion transport path (Figure 5c). In addition, the reduction of hydroxyl terminal groups resulting from annealing would further accelerate ion transport within the layer [35]. This structure improvement is confirmed by the significant reduction in resistance detected in the PS-MXene film compared to the vacuum-filtered MXene film (Figure S7a). The PS-MXene also shows a much higher specific capacity (90.0 mAh g^{-1}) compared to the $\text{Ti}_3\text{C}_2\text{T}_x$ without PS treatment (72.0 mAh g^{-1}) at 1 A g^{-1} , as shown in Figures S6 and S7b.

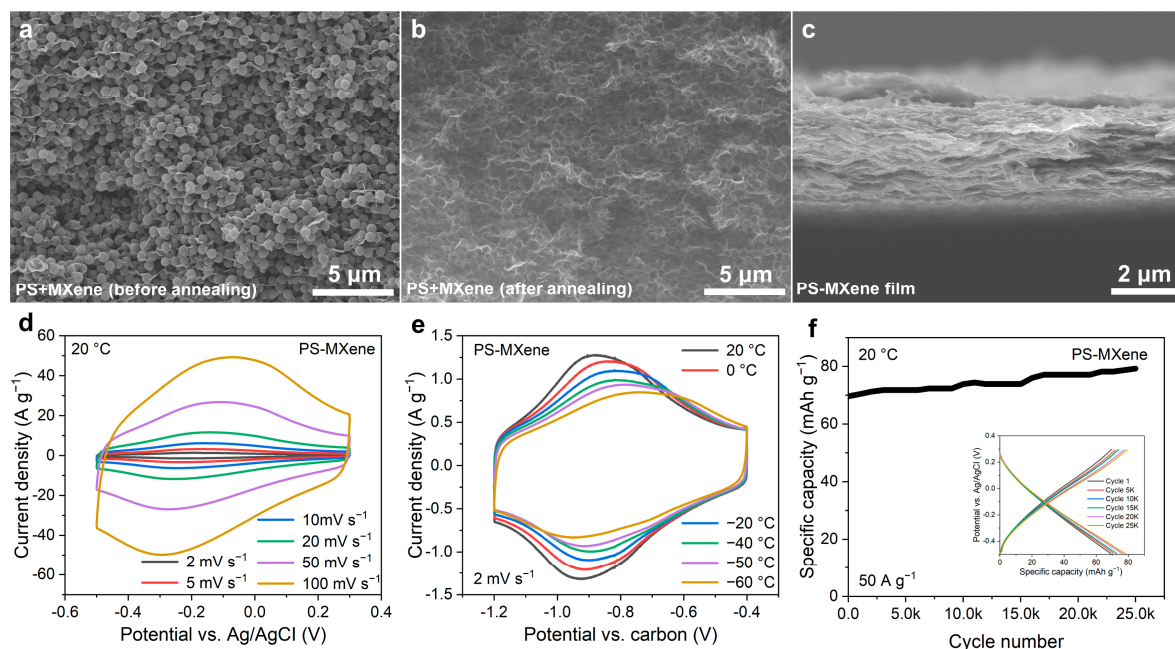


Figure 5. Morphology and electrochemical characterization of PS-MXene in 9.5 M H_3PO_4 . SEM images of PS+MXene vacuum-filtered film (a) before and (b) after annealing. (c) Cross-section SEM images of PS-MXene film. Cyclic voltammograms of the PS-MXene electrode measured (d) at 20 °C at different scan rates and (e) at different temperatures with a scan rate of 2 mV s^{-1} . (f) Capacity retention test of the PS-MXene electrode. The inset shows galvanostatic cycling data at 50 A g^{-1} .

The CV curves of PS-MXene show only a slight shift with increasing scan rates from 10 to 100 mV s^{-1} , indicating the maintenance of fast redox reaction even at 100 mV s^{-1} (Figure 5d). Furthermore, ~60 mAh g^{-1} specific capacity is retained at 100 A g^{-1} (Figure S7b). Moreover, the structure improvement also enhances the low-temperature performance of the electrode, albeit with a notable decrease in pseudo-capacitance. Nevertheless, ~70% specific capacitance is maintained when the temperature decreases to −60 °C at 2 mV s^{-1} (Figure 5e). These suggest an excellent high-rate performance of the electrode in a wide range of temperatures. In addition, PS-MXene exhibits excellent electrochemical stability in the H_3PO_4 electrolyte. After 25,000 cycles at 20 °C, the PS-MXene electrode exhibits no degradation; instead, it shows a slight increase in specific capacity (Figure 5f). In summary, the product PS-MXene electrode has improved structure, achieving high power, high capacity, and high cycling stability simultaneously.

To match the H^+ storage capability of MXene, a cathode with abundant H^+ is required. In this study, H-TBA was used as the positive electrode material [28], known for its contiguous network of hydrogen-bonded lattice water [25] and a large concentration of protons. As shown in Figure 6a, only a slight change can be detected between the XRD patterns of pristine TBA and H-TBA, attributed to the small size of H^+ . Moreover, the morphology of TBA remains intact post-protonation, with particles uniformly distributed and exhibiting a diameter of about 50 nm (Figure 6b,c). This particle structure shortens the transport paths, thus facilitating H^+ transport via the Grotthuss mechanism. In addition, owing to its particle structure and excellent hydrophilicity, similar electrochemical performance is observed in 5 M H_2SO_4 and 9.5 M H_3PO_4 electrolyte (Figures S8a and S8b). The only discernible difference lies in the ohmic resistance, primarily due to the electrolyte conductivity (Figure S8c). Thus, excellent rate performance and low-temperature tolerance are anticipated for H-TBA in 9.5 M H_3PO_4 .

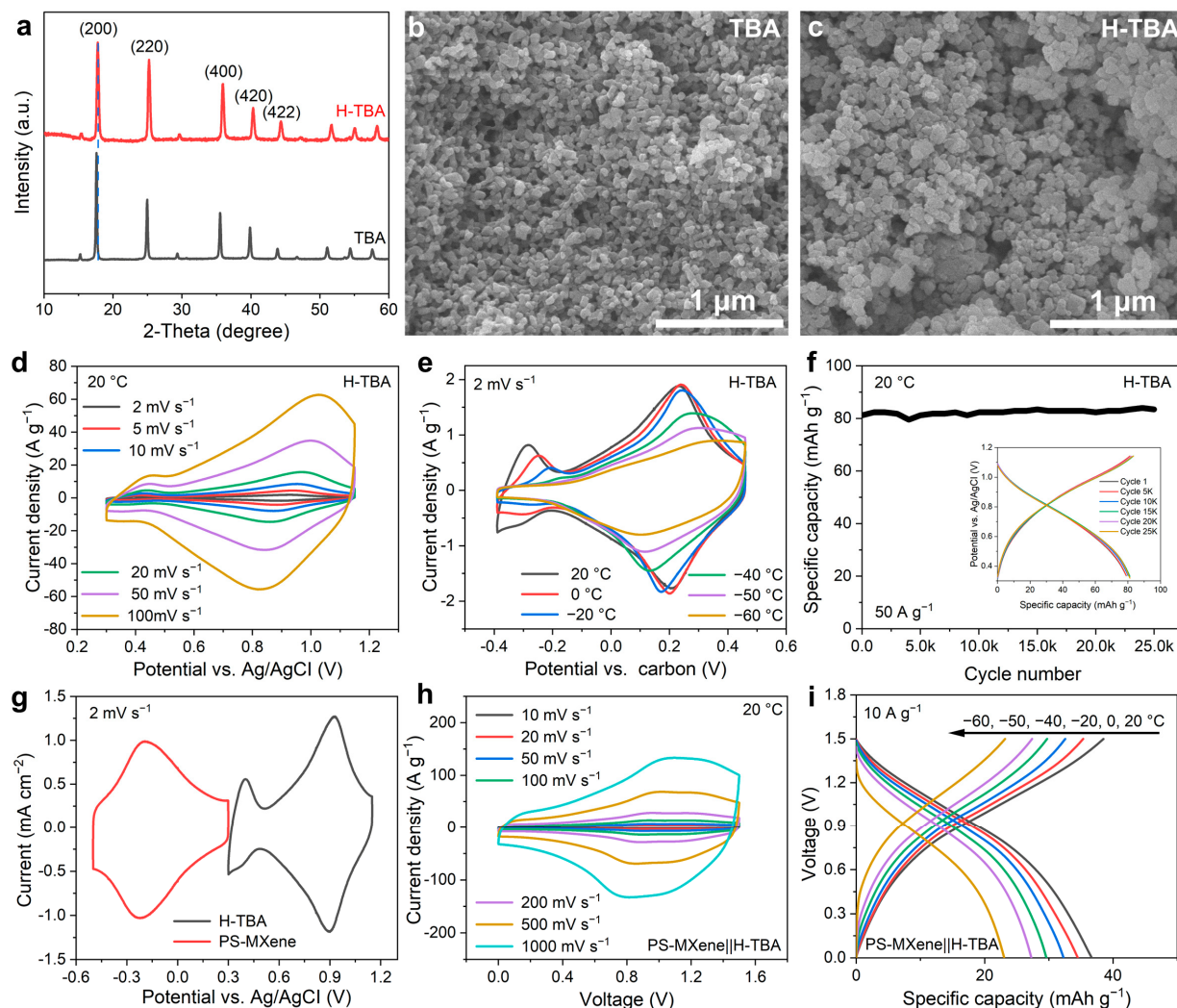


Figure 6. Characterization of H-TBA and electrochemical performance of PS-MXene || H-TBA proton battery in 9.5 M H_3PO_4 . (a) XRD patterns of TBA and H-TBA. SEM images of (b) TBA and (c) H-TBA. CV plots of the H-TBA electrode measured (d) at 20 °C with different scan rates and (e) at different temperatures with a scan rate of 2 mV s⁻¹. (f) Capacity retention of the H-TBA electrode. The inset shows galvanostatic cycling data at 50 A g⁻¹. (g) Full cell fabrication: three-electrode CV plots of PS-MXene (0.7 mg cm⁻²) and H-TBA (0.75 mg cm⁻²) at 2 mV s⁻¹. (h) CV plots of the PS-MXene || H-TBA aqueous proton battery at different scan rates. (i) GCD profiles measured at different temperatures with a current density of 10 A g⁻¹.

Similar to PS-MXene, H-TBA also maintains a fast redox reaction, as evidenced by capacity retention of over 70% at 100 A g⁻¹ (Figures 6d and S8f). Moreover, H-TBA performs well even at -60 °C (Figures 6e and S8). Its excellent cycling stability and suitable potential window make H-TBA a promising positive electrode material in proton batteries to pair with PS-MXene (Figure 6f,g). The product PS-MXene || H-TBA proton battery exhibits outstanding rate performance, with the CV curve maintaining its shape even at 500 mV s⁻¹. Approximately 30 mAh g⁻¹ specific capacity (~26 Wh kg⁻¹ energy density and 162 kW kg⁻¹ power density, based on the total mass of PS-MXene and H-TBA) is achieved at 200 A g⁻¹ (Figure 6h). That is because charge transfer is only related to H^+ , and the path for ion transfer in the product proton device is short. Consequently, the low-temperature tolerance of the PS-MXene || H-TBA proton battery is improved compared to the half-cell performance of individual PS-MXene and H-TBA. More than half of the specific capacity (~23 mAh g⁻¹, ~17 Wh kg⁻¹ energy density and 7.4 kW kg⁻¹ power density) is maintained at a low temperature of -60 °C and a high current density of 10 A g⁻¹.

(Figure 6i). In addition, the PS-MXene || H-TBA proton battery achieves no decay after 3000 cycles, indicating excellent cycling stability even at low temperatures (Figure S9). It is noted that for capacitance material, self-discharge rate is a key parameter. Due to the influence of self-discharge, the charging and discharging efficiency of PS-MXene || H-TBA proton battery at room temperature is about 95% at 10 A g^{-1} and alleviates with decreasing temperature. The high self-discharge rate at room temperature might be caused by the low mass loading, which could also be alleviated like a supercapacitor with increasing mass loading.

4. Conclusions

This study sheds light on the charge transport mechanisms of $\text{Ti}_3\text{C}_2\text{T}_x$ in acid electrolytes and explores its potential application in proton batteries. Through a combination of EQCM tests and computational methods such as DFT and MD simulations, we elucidated that the ion transport mechanisms in $\text{Ti}_3\text{C}_2\text{T}_x$ MXene are the same in H_2SO_4 and H_3PO_4 electrolytes; both proton (Grutthuss mechanism) and hydronium ion (Vehicle mechanism) transfers occur during charge and discharge due to differences in terminal groups. Specifically, the hydrogen bonding network formed by water molecules adsorbed by hydroxyl functional groups under van der Waals forces enables charge transfer in the form of naked H^+ through the Grutthuss mechanism. In contrast, the hydrophobic channel formed by oxygen and halogen terminal groups facilitates rapid charge transfers in the form of hydronium ion via the Vehicle mechanism, owing to negligible interfacial effect. This energy storage mechanism enables the development of a porous hydroxy-poor $\text{Ti}_3\text{C}_2\text{T}_x$ MXene || H-TBA proton battery with excellent rate performance, low-temperature tolerance, and cycling stability.

Overall, this investigation highlights the potential of MXene-based materials in advancing the development of high-performance energy storage devices and provides valuable insights into their charge storage mechanisms in acid electrolytes. Further research in this direction could lead to the commercialization of efficient and sustainable energy storage solutions for various applications.

Supplementary Materials: The following supporting information can be downloaded at: <https://www.mdpi.com/article/10.3390/batteries10060207/s1>, Scheme S1: Synthesis scheme of the vacuum-filtered $\text{Ti}_3\text{C}_2\text{T}_x$ film electrode and assembly schematic of the proton battery. Figure S1: (a) Dingdall phenomenon of diluted few-layer $\text{Ti}_3\text{C}_2\text{T}_x$ colloidal solution. (b) Optical image of the vacuum-filtered $\text{Ti}_3\text{C}_2\text{T}_x$ MXene film. The film exhibits excellent flexibility. Figure S2: (a) CV profile and electrode mass response and (b) electrode mass change versus charge for $\text{Ti}_3\text{C}_2\text{T}_x$ MXene on an Au-coated quartz crystals substrate recorded at 10 mV s^{-1} with a potential range of 0.05 to 0.25 V in 9.5 M H_3PO_4 . Figure S3: Adsorption energy of H_2O on the surface of (a) $\text{Ti}_3\text{C}_2\text{O}_2$, (b) $\text{Ti}_3\text{C}_2\text{F}_2$, (c) $\text{Ti}_3\text{C}_2\text{Cl}_2$, and (d) $\text{Ti}_3\text{C}_2(\text{OH})_2$. Figure S4: Cyclic voltammograms of the $\text{Ti}_3\text{C}_2\text{T}_x$ MXene film electrode measured at different scan rates in 5 M H_2SO_4 . Figure S5: Fitted EIS plots shown in Figure 4d and 4e using Zview software (2.6.0.11). Figure S6: Specific gravimetric capacity vs. current density for $\text{Ti}_3\text{C}_2\text{T}_x$ MXene film electrode measured at different temperatures in 9.5 M H_3PO_4 . Figure S7: (a) Electrochemical impedance spectroscopy of the $\text{Ti}_3\text{C}_2\text{T}_x$ MXene and PS-MXene film electrodes collected at 0.2 V vs. Ag/AgCl in 9.5 M H_3PO_4 . The inset shows the high-frequency range. (b) Specific gravimetric capacity vs. current density for PS-MXene film electrode at different temperatures. Figure S8: Electrochemical performance of H-TBA in acid electrolyte. (a) Cyclic voltammograms of H-TBA at a scan rate of 2 mV s^{-1} in 5 M H_2SO_4 and 9.5 M H_3PO_4 , respectively. (b) Galvanostatic charge-discharge profiles of H-TBA at a current density of 1 A g^{-1} in 5 M H_2SO_4 and 9.5 M H_3PO_4 . (c) Electrochemical impedance spectroscopy of H-TBA collected at 0.8 V vs. Ag/AgCl in 5 M H_2SO_4 and 9.5 M H_3PO_4 . The inset shows the high-frequency range. (d) Galvanostatic cycling profiles of H-TBA at different temperatures with current density of 1 A g^{-1} in 9.5 M H_3PO_4 . (e) Electrochemical impedance spectroscopy data of H-TBA collected at 0.1 V vs. carbon at different temperatures in 9.5 M H_3PO_4 . The inset shows the high-frequency range. (f) Specific gravimetric capacity vs. current density for H-TBA at different temperatures. Figure S9: Electrochemical performance of PS-MXene || H-TBA proton battery in 9.5 M H_3PO_4 . (a) Galvanostatic charge-discharge profiles of proton battery measured at 20 °C with

(a) current densities of 5, 10, 20, 50, 100, 200 A g⁻¹ and (b) -60 °C with current densities of 0.2, 0.5, 2, 5, 10 A g⁻¹. (c) Capacity retention of PS-MXene || H-TBA proton battery at -60 °C. The inset shows galvanostatic cycling data collected at 10 A g⁻¹. Table S1: Comparison of some previous studies that used acidic electrolyte [38].

Author Contributions: Conceptualization, J.X.; Methodology, X.L. and B.H.; Writing—original draft, J.Z.; Writing—review & editing, S.G.; Supervision, J.X. All authors have read and agreed to the published version of the manuscript.

Funding: This work was financially supported by the National Natural Science Foundation of China (22005124) and Special Fund for Science and Technology Innovation of Jiangsu Province (BE2022610).

Data Availability Statement: The original contributions presented in the study are included in the article, further inquiries can be directed to the corresponding authors.

Conflicts of Interest: There are no conflicts to declare.

References

1. Simon, P.; Gogotsi, Y. Materials for electrochemical capacitors. *Nat. Mater.* **2008**, *7*, 845–854. [[CrossRef](#)] [[PubMed](#)]
2. Simon, P.; Gogotsi, Y.; Dunn, B. Where do batteries end and supercapacitors begin? *Science* **2014**, *343*, 1210–1211. [[CrossRef](#)] [[PubMed](#)]
3. Zhu, Y.; Murali, S.; Stoller, M.D.; Ganesh, K.J.; Cai, W.; Ferreira, P.J.; Pirkle, A.; Wallace, R.M.; Cychosz, K.A.; Thommes, M.; et al. Carbon-Based Supercapacitors Produced by Activation of Graphene. *Science* **2011**, *332*, 1537–1541. [[CrossRef](#)] [[PubMed](#)]
4. Mathis, T.S.; Kurra, N.; Wang, X.; Pinto, D.; Simon, P.; Gogotsi, Y. Energy Storage Data Reporting in Perspective-Guidelines for Interpreting the Performance of Electrochemical Energy Storage Systems. *Adv. Energy Mater.* **2019**, *9*, 1902007. [[CrossRef](#)]
5. Augustyn, V.; Simon, P.; Dunn, B. Pseudocapacitive oxide materials for high-rate electrochemical energy storage. *Energy Environ. Sci.* **2014**, *7*, 1597–1614. [[CrossRef](#)]
6. Zhong, C.; Deng, Y.; Hu, W.; Qiao, J.; Zhang, L.; Zhang, J. A review of electrolyte materials and compositions for electrochemical supercapacitors. *Chem. Soc. Rev.* **2015**, *44*, 7484–7539. [[CrossRef](#)] [[PubMed](#)]
7. Chen, L.Y.; Hou, Y.; Kang, J.L.; Hirata, A.; Fujita, T.; Chen, M.W. Toward the Theoretical Capacitance of RuO₂ Reinforced by Highly Conductive Nanoporous Gold. *Adv. Energy Mater.* **2013**, *3*, 851–856. [[CrossRef](#)]
8. Tang, H.; Chen, W.; Li, N.; Hu, Z.; Xiao, L.; Xie, Y.; Xi, L.; Ni, L.; Zhu, Y. Layered MnO₂ nanodots as high-rate and stable cathode materials for aqueous zinc-ion storage. *Energy Storage Mater.* **2022**, *48*, 335–343. [[CrossRef](#)]
9. Russell, J.C.; Posey, V.A.; Gray, J.; May, R.; Reed, D.A.; Zhang, H.; Marbella, L.E.; Steigerwald, M.L.; Yang, Y.; Roy, X.; et al. High-performance organic pseudocapacitors via molecular contortion. *Nat. Mater.* **2021**, *20*, 1136–1141. [[CrossRef](#)] [[PubMed](#)]
10. Boota, M.; Gogotsi, Y. MXene—Conducting Polymer Asymmetric Pseudocapacitors. *Adv. Energy Mater.* **2019**, *9*, 1802917. [[CrossRef](#)]
11. Sun, H.; Mei, L.; Liang, J.; Zhao, Z.; Lee, C.; Fei, H.; Ding, M.; Lau, J.; Li, M.; Wang, C.; et al. Three-dimensional holey-graphene/niobia composite architectures for ultrahigh-rate energy storage. *Science* **2017**, *356*, 599–604. [[CrossRef](#)] [[PubMed](#)]
12. Lang, X.; Hirata, A.; Fujita, T.; Chen, M. Nanoporous metal/oxide hybrid electrodes for electrochemical supercapacitors. *Nat. Nanotechnol.* **2011**, *6*, 232–236. [[CrossRef](#)] [[PubMed](#)]
13. Kim, H.-S.; Cook, J.B.; Tolbert, S.H.; Dunn, B. The development of pseudocapacitive properties in nanosized-MoO₂. *J. Electrochem. Soc.* **2015**, *162*, A5083–A5090. [[CrossRef](#)]
14. Feng, D.; Lei, T.; Lukatskaya, M.R.; Park, J.; Huang, Z.; Lee, M.; Shaw, L.; Chen, S.; Yakovenko, A.A.; Kulkarni, A.; et al. Robust and conductive two-dimensional metal–organic frameworks with exceptionally high volumetric and areal capacitance. *Nat. Energy* **2018**, *3*, 30–36. [[CrossRef](#)]
15. Xu, J.; Hu, X.; Wang, X.; Wang, X.; Ju, Y.; Ge, S.; Lu, X.; Ding, J.; Yuan, N.; Gogotsi, Y. Low-temperature pseudocapacitive energy storage in Ti₃C₂Tx MXene. *Energy Storage Mater.* **2020**, *33*, 382–389. [[CrossRef](#)]
16. Anasori, B.; Lukatskaya, M.R.; Gogotsi, Y. 2D metal carbides and nitrides (MXenes) for energy storage. *Nat. Rev. Mater.* **2017**, *2*, 16098. [[CrossRef](#)]
17. Lukatskaya, M.R.; Mashtalir, O.; Ren, C.E.; Dall’agnese, Y.; Rozier, P.; Taberna, P.L.; Naguib, M.; Simon, P.; Barsoum, M.W.; Gogotsi, Y. Cation Intercalation and High Volumetric Capacitance of Two-Dimensional Titanium Carbide. *Science* **2013**, *341*, 1502–1505. [[CrossRef](#)] [[PubMed](#)]
18. Ghidiu, M.; Lukatskaya, M.R.; Zhao, M.-Q.; Gogotsi, Y.; Barsoum, M.W. Conductive two-dimensional titanium carbide ‘clay’ with high volumetric capacitance. *Nature* **2014**, *516*, 78–81. [[CrossRef](#)] [[PubMed](#)]
19. Lukatskaya, M.R.; Kota, S.; Lin, Z.; Zhao, M.-Q.; Shpigel, N.; Levi, M.D.; Halim, J.; Taberna, P.-L.; Barsoum, M.W.; Simon, P.; et al. Ultra-high-rate pseudocapacitive energy storage in two-dimensional transition metal carbides. *Nat. Energy* **2017**, *2*, 17105. [[CrossRef](#)]
20. Liu, F.; Liu, Y.; Zhao, X.; Liu, X.; Fan, L.-Z. Pursuit of a high-capacity and long-life Mg-storage cathode by tailoring sandwich-structured MXenes@carbon nanosphere composites. *J. Mater. Chem. A* **2019**, *7*, 16712–16719. [[CrossRef](#)]

21. Emanuelsson, R.; Sterby, M.; Strømme, M.; Sjödin, M. An All-Organic Proton Battery. *J. Am. Chem. Soc.* **2017**, *139*, 4828–4834. [[CrossRef](#)] [[PubMed](#)]
22. Tomai, T.; Mitani, S.; Komatsu, D.; Kawaguchi, Y.; Honma, I. Metal-free aqueous redox capacitor via proton rocking-chair system in an organic-based couple. *Sci. Rep.* **2014**, *4*, 3591. [[CrossRef](#)] [[PubMed](#)]
23. Guo, Z.; Huang, J.; Dong, X.; Xia, Y.; Yan, L.; Wang, Z.; Wang, Y. An organic/inorganic electrode-based hydronium-ion battery. *Nat. Commun.* **2020**, *11*, 959. [[CrossRef](#)] [[PubMed](#)]
24. Agmon, N. The Grotthuss mechanism. *Chem. Phys. Lett.* **1995**, *244*, 456–462. [[CrossRef](#)]
25. Wu, X.; Hong, J.J.; Shin, W.; Ma, L.; Liu, T.; Bi, X.; Yuan, Y.; Qi, Y.; Surta, T.W.; Huang, W.; et al. Diffusion-free Grotthuss topochemistry for high-rate and long-life proton batteries. *Nat. Energy* **2019**, *4*, 123–130. [[CrossRef](#)]
26. Wang, X.; Xu, J.; Razal, J.M.; Yuan, N.; Zhou, X.; Wang, X.; Ding, J.; Qin, S.; Ge, S.; Gogotsi, Y. Unimpeded migration of ions in carbon electrodes with bimodal pores at an ultralow temperature of $-100\text{ }^{\circ}\text{C}$. *J. Mater. Chem. A* **2019**, *7*, 16339–16346. [[CrossRef](#)]
27. Xu, J.; Yuan, N.; Razal, J.M.; Zheng, Y.; Zhou, X.; Ding, J.; Cho, K.; Ge, S.; Zhang, R.; Gogotsi, Y.; et al. Temperature-independent capacitance of carbon-based supercapacitor from -100 to $60\text{ }^{\circ}\text{C}$. *Energy Storage Mater.* **2019**, *22*, 323–329. [[CrossRef](#)]
28. Jiang, H.; Shin, W.; Ma, L.; Hong, J.J.; Wei, Z.; Liu, Y.; Zhang, S.; Wu, X.; Xu, Y.; Guo, Q.; et al. A high-rate aqueous proton battery delivering power below $-78\text{ }^{\circ}\text{C}$ via an unfrozen phosphoric acid. *Adv. Energy Mater.* **2020**, *10*, 2000968. [[CrossRef](#)]
29. Lukatskaya, M.R.; Bak, S.; Yu, X.; Yang, X.; Barsoum, M.W.; Gogotsi, Y. Probing the Mechanism of High Capacitance in 2D Titanium Carbide Using In Situ X-ray Absorption Spectroscopy. *Adv. Energy Mater.* **2015**, *5*, 1500589. [[CrossRef](#)]
30. Mu, X.; Wang, D.; Du, F.; Chen, G.; Wang, C.; Wei, Y.; Gogotsi, Y.; Gao, Y.; Dall’Agnese, Y. Revealing the Pseudo-Intercalation Charge Storage Mechanism of MXenes in Acidic Electrolyte. *Adv. Funct. Mater.* **2019**, *29*, 201902953. [[CrossRef](#)]
31. Zhan, C.; Naguib, M.; Lukatskaya, M.; Kent, P.R.C.; Gogotsi, Y.; Jiang, D.-E. Understanding the MXene Pseudocapacitance. *J. Phys. Chem. Lett.* **2018**, *9*, 1223–1228. [[CrossRef](#)] [[PubMed](#)]
32. Park, S.H.; Kim, J.; Lee, W.-E.; Byun, D.-J.; Kim, M.H. One-Step Synthesis of Hollow Dimpled Polystyrene Microparticles by Dispersion Polymerization. *Langmuir* **2017**, *33*, 2275–2282. [[CrossRef](#)] [[PubMed](#)]
33. Zhang, X.; Liu, X.; Feng, Y.; Qiu, S.; Shao, Y.; Liao, Q.; Li, H.; Liu, Y. In situ Modified Mesoporous MXene Film with Excellent Oxidation Resistance for High-Performance Supercapacitor. *Appl. Mater. Today* **2022**, *27*, 101483. [[CrossRef](#)]
34. Chen, X.; Zhu, Y.; Zhang, M.; Sui, J.; Peng, W.; Li, Y.; Zhang, G.; Zhang, F.; Fan, X. N-butyllithium-treated Ti₃C₂T_x MXene with excellent pseudocapacitor performance. *ACS Nano* **2019**, *13*, 9449–9456. [[CrossRef](#)] [[PubMed](#)]
35. Shao, H.; Xu, K.; Wu, Y.-C.; Iadecola, A.; Liu, L.; Ma, H.; Qu, L.; Raymundo-Piñero, E.; Zhu, J.; Lin, Z.; et al. Unraveling the Charge Storage Mechanism of Ti₃C₂T_x MXene Electrode in Acidic Electrolyte. *ACS Energy Lett.* **2020**, *5*, 2873–2880. [[CrossRef](#)]
36. Tsai, W.-Y.; Taberna, P.-L.; Simon, P. Electrochemical Quartz Crystal Microbalance (EQCM) Study of Ion Dynamics in Nanoporous Carbons. *J. Am. Chem. Soc.* **2014**, *136*, 8722–8728. [[CrossRef](#)] [[PubMed](#)]
37. Xu, J.; Zhang, R.; Chen, P.; Ge, S. Effects of adding ethanol to KOH electrolyte on electrochemical performance of titanium carbide-derived carbon. *J. Power Sources* **2014**, *246*, 132–140. [[CrossRef](#)]
38. Yan, L.; Huang, J.; Guo, Z.; Dong, X.; Wang, Z.; Wang, Y. Solid-State Proton Battery Operated at Ultralow Temperature. *ACS Energy Lett.* **2020**, *5*, 685–691. [[CrossRef](#)]

Disclaimer/Publisher’s Note: The statements, opinions and data contained in all publications are solely those of the individual author(s) and contributor(s) and not of MDPI and/or the editor(s). MDPI and/or the editor(s) disclaim responsibility for any injury to people or property resulting from any ideas, methods, instructions or products referred to in the content.